Geomechanics and Engineering, *Vol. 43, No. 2 (2025) 141-153*
https://doi.org/10.12989/gae.2025.43.2.141

Effect of bedding plane strength on the bending fracture behaviour of soft-hard interbedded rock layers

Yang Liu[1], Da Huang*[2] and Hao Li[1]

[1]*School of Architectural Engineering, Sichuan Polytechnic University, No. 801, SEC. 2, Taishan South Road, Deyang, 618000, Sichuan, China*
[2]*College of Geology Engineering and Geomatics, Chang'an University, 126 Yanta Road, Xi 'an, 710054, Shanxi, China*

(*Received November 7, 2024, Revised October 6, 2025, Accepted October 14, 2025*)

Abstract. Bending fracture is a dominant failure pattern of soft-hard interbedded rock layers (SHIRLs). This study investigated the influence of bedding plane strength on the bending fracture behavior of SHIRLs using three-point-bending (TPB) tests and digital image correlation (DIC) technology. The test results indicate that the higher bedding plane strength reduces the dispersion of load-displacement curves, fracture displacement, fracture load and failure patterns. Specifically, in SHIRLs with strong bedding planes, the fracture load increases linearly with bedding plane strength, whereas the fracture displacement decreases linearly. In these cases, the instantaneous length of the main crack is approximately half of the sample. Conversely, in SHIRLs with weak bedding planes, the load-displacement curves, fracture displacement, fracture load and instantaneous crack length all exhibit significant dispersion. Particle flow code (PFC^{2D}) is an effective numerical analysis method for exploring the bending fracture behavior of SHIRL under TPB test. Numerical simulation results further show that the bedding plane strength have significant impact on the fracture load, failure pattern and the proportion of tensile versus shear cracks. The findings of this study can provide theoretical reference and guidance for the reinforcement of SHIRLs.

Keywords: bending fracture; particle flow code; soft-hard interbedded rock layers; three-point-bending test

1. Introduction

Layered rock masses are prevalent in nature and constitute the majority of sedimentary rocks and a significant portion of metamorphic rocks (Doolin and Mauldon 2001, Mohammadi and Hossaini 2017, Son *et al*. 2017, Meier *et al*. 2017, Zolfaghari *et al*. 2024, Terron-Almenara *et al*. 2024). SHIRLs represent a distinct category of such masses, characterized by alternating sequences of hard and soft rock layers. The mechanical properties of these layers differ substantially. Hard rock layers are denser, possess superior mechanical strength, and exhibit lower deformability. In contrast, soft rock layers are less dense, have inferior mechanical properties, and are more susceptible to larger deformations. Furthermore, numerous model tests and case studies have identified bending fracture as a predominant failure pattern in SHIRLs (Gu and Huang 2016, Dong *et al*. 2020a, b, Chen *et al*. 2020, Khalili *et al*. 2023), exemplified by the toppling failure of anti-dip slopes (Fig. 1(a)) and the roof bending failure in tunnels (Fig. 1(b)).

The mechanical behavior of soft-hard interbedded rock layers (SHIRLs) has been investigated using Brazilian tests, uniaxial and triaxial compression tests, and dynamic compression tests. These studies have primarily focused on how the dip angle and spatial position of the layered structure influence mechanical behavior. For instance, Hu *et al*. (2019) demonstrated that the rock layer dip angle significantly affects the failure pattern of SHIRLs. Similarly, Luo *et al*. (2021) found that the viscoelastic deformation of SHIRLs is controlled by both the volume ratio of the rock layers and the spatial position of the layered structure. While numerous studies have examined bending fracture in layered rock masses, they have predominantly focused on unitary lithologies such as sandstone, shale, or rock-like materials. The three-point-bending (TPB) test is a standard method for studying rock fracture. For example, Khalili *et al*. (2023) used rock-like materials in TPB tests to show that bedding planes alter the crack propagation mechanism, shifting the fracture mode from a pure opening mode in isotropic specimens to mixed modes at various bedding angles. In a semicircular bending study on sandstone, Huang *et al*. (2020) reported that fracture patterns are primarily governed by the dip angle and partially influenced by bedding plane strength and spacing. Likewise, Liu *et al*. (2019) employed TPB tests and digital image correlation (DIC) on shale, concluding that bedding plane strength governs both the crack propagation path and strain distribution.

In addition, the Particle Flow Code (PFC^{2D}) is an effective numerical method for investigating fracture mechanisms in layered rock masses. For instance, Singh *et al*. (2024) used PFC^{2D} to simulate Brazilian tensile strength tests on intact, foliated, and pre-cracked rocks, finding that crack initiation consistently occurred at the foliation nearest to the sample's center. Similarly, Wen *et al*. (2020) combined split Hopkinson pressure bar (SHPB) tests with

*Corresponding author, Professor
E-mail: huangda@chd.edu.cn

ISSN: 2005-307X (Print), 2092-6219 (Online)

Table 1 The weight ratio of composition materials of soft and hard rock

Types	Quartz sand	Barite powder	Cement	Gypsum	kaolin	water-binder ratio
Soft rock	0.8	0.2	2	0.4	0.3	0.42
Hard rock	3.2	0.8	2.1	0.9	1	0.83

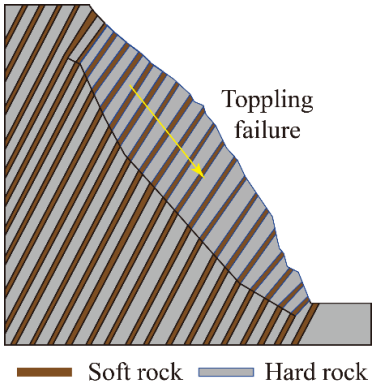

(a) Toppling failure of anti-dip rock slope (Gu and Huang 2016)

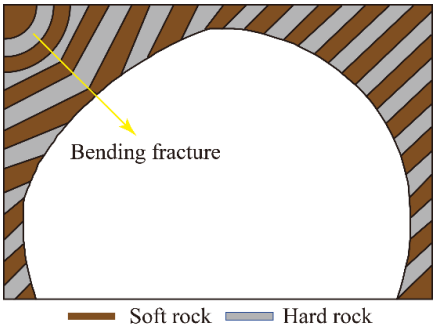

(b) Bending failure of wall of tunnel (Chen *et al*. 2020)

Fig. 1 Typical bending failure of soft-hard interbedded roc layers

PFC^{2D} simulations to study layered rock with significant interlayer strength contrasts; their numerical analysis allowed the investigation of dynamic characteristics across a broader range of strain rates and dip angles. In a study on shale, Dou *et al*. (2019) employed PFC^{2D} to model notched three-point-bending tests and demonstrated that joint parameters significantly influence tensile strength, fracture toughness, and failure patterns. Furthermore, Guo *et al*. (2018) systematically explored the influence of coal thickness on the mechanical behavior of rock-coal-rock composites using PFC^{2D} simulations of compression tests. Their results indicated that the samples' deformation and strength depend not only on coal thickness but also on confining pressure.

Current research on the mechanical behaviour of SHIRLs has primarily focused on compressive, tensile, and dynamic compressive failure. In **parallel**, investigations into the bending fracture of layered rock masses have chiefly examined formations of a unitary lithology, such as layered sandstone or shale. Consequently, the bending fracture behaviour of SHIRLs remains insufficiently studied, and the underlying mechanisms are not well understood. This study addresses this gap by preparing hard and soft rocks with significantly different mechanical properties using rock-like materials, as well as SHIRL samples with varying bedding plane strengths. The fracture process-including crack initiation and propagation-in SHIRLs under TPB tests was analyzed using digital image correlation (DIC) technology. Furthermore, the influence of bedding plane strength on bending fracture behavior was investigated numerically through PFC^{2D} simulations.

2. Methods

2.1 Three-point-bending test

2.1.1 Materials

Rock-like materials are widely employed in rock mechanics and model tests due to their mechanical properties, which closely resemble those of natural rock (Haeri *et al*. 2015, Alitalesh *et al*. 2020, Sharafisafa *et al*. 2021, Lee *et al*. 2023, Kumar *et al*. 2023). Moreover, fabricating layered rock masses with specific layer thicknesses and bedding plane strengths directly from natural rock is often impractical. The mechanical properties of rock-like materials, by contrast, can be precisely controlled by adjusting the weight ratios of their constituents. Consequently, these materials are an ideal choice for preparing SHIRLs samples. In this study, the constituent materials for the soft and hard rock analogs include quartz sand, barite powder, cement, gypsum, and kaolin. The specific weight ratios for these compositions are provided in Table 1.

2.1.2 Sample preparation

To prepare SHIRL samples with varying layer thicknesses and bedding plane strengths, a custom metal mold was designed, as illustrated in Fig. 2(a). The mold assembly comprises five rectangular steel plates, four steel angles, and several detachable steel bars. A base plate measuring 330 mm (length) × 180 mm (width) × 4 mm (thickness) forms the foundation. Four steel angles are welded to the corners of this base plate. Along the length of the base plate, two side plates (330 mm × 100 mm × 4 mm) are welded along the inside of the steel angles (Fig. 2(c)). The side plate and the adjacent steel angle form a groove on each side, into which the ends of the detachable steel bars can be inserted (Fig. 2(d)). The height of these bars strictly controls the thickness of each rock layer. Furthermore, two vertical partition plates (330 mm × 100 mm × 4 mm) are welded onto the base plate with a fixed spacing of 60 mm between them. These partitions enable the direct casting of the designed SHIRL samples, eliminating the need for post-casting cutting. This approach simplifies the preparation process and avoids potential damage to the internal structure from cutting.

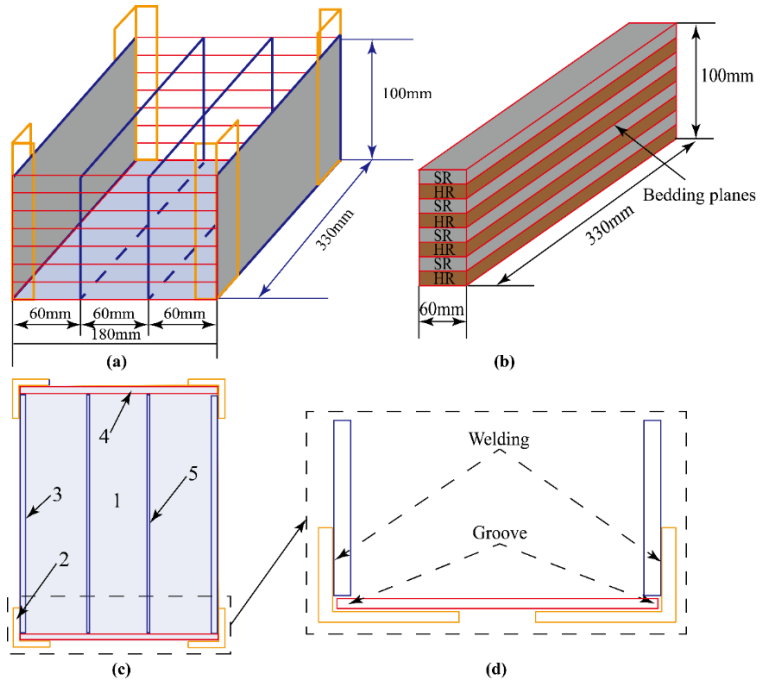

1 the bottom rectangular steel plate 2 the steel angles
3 the steel plate 4 the detachable steel bar
5 the vertical partition plate

Fig. 2 Schematic diagram of the mold for SHIRLs: (a) size of main structure, (b) the size of sample, (c) the top view of main structure and (d) the grooves that can install the detachable steel bar

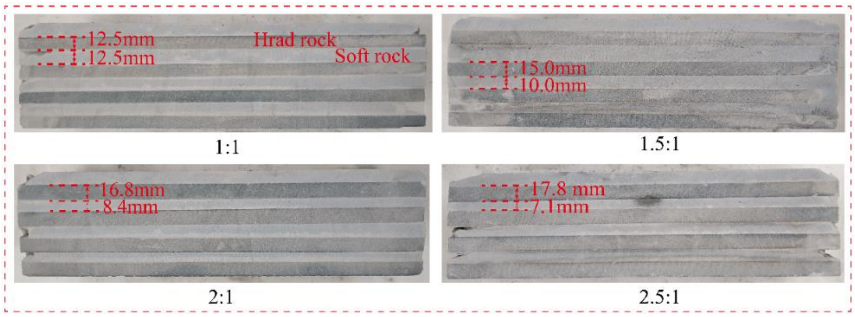

(a) Weak bedding plane strength

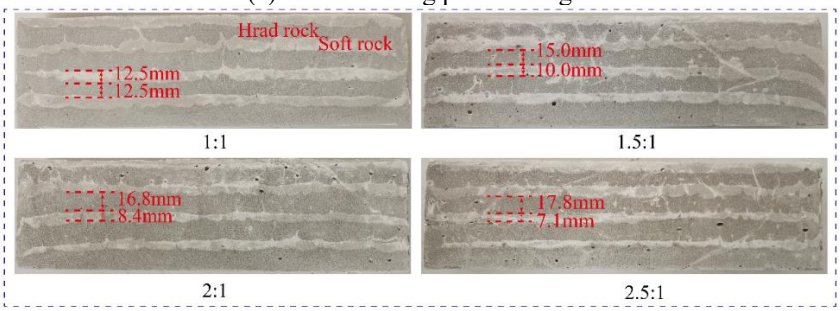

(b) Strong bedding plane strength

Fig. 3 Two types of SHIRLs with different bedding plane strength

The SHIRL configuration, detailed in Fig. 2(b), consists of four hard rock layers and four soft rock layers. Based on extensive field surveys showing that hard rock layers in SHIRLs are typically thicker than soft rock layers, the totalsample height was fixed at 100 mm. Four different layer thickness ratios (defined as the ratio of hard rock layer thickness to soft rock layer thickness) were designed: 1:1 (12.5 mm : 12.5 mm), 1.5:1 (15 mm : 10 mm), 2:1 (16.8 mm : 8.4 mm), and 2.5:1 (17.8 mm : 7.1 mm).

The detailed preparation process for the SHIRLs was as follows:

Table 2 Basic mechanical parameters of hard rock and soft rock

Types	Uniaxial compression strength (MPa)	Tensile strength (MPa)	Elasticity modulus (GPa)	Poisson's ratio	Cohesive force (kN)	Internal friction angle (°)
Hard rock	19.01	2.63	3.19	0.27	3.18	20.24
Soft rock	4.25	0.98	1.01	0.33	1.81	6.47

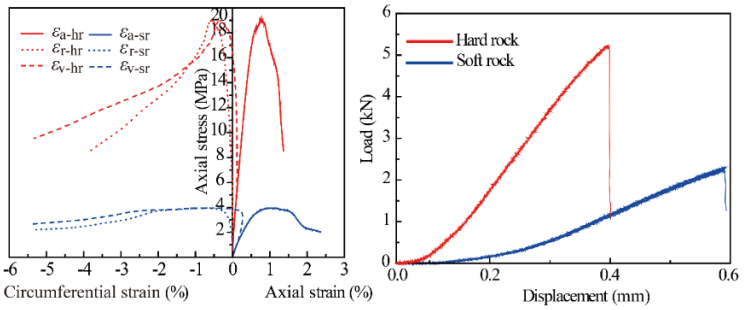

(a) Uniaxial compression test of soft and hard rock (b) Brazilian disc test of soft and hard rock

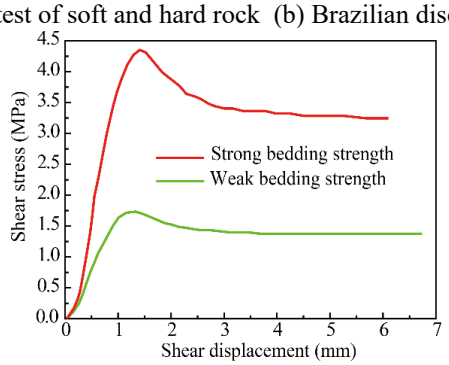

(c) Direct shear test of bedding planes

Fig. 4 The mechanical properties test of soft rock, hard rock and bedding planes

Casting. The metal mold was first lubricated and lined with a layer of plastic film to facilitate demolding after the mortar solidified. The first detachable steel bar was then installed, and the hard rock mixture mortar was poured into the mold. The bedding plane strength was controlled by varying the time interval between pouring successive rock layers. For samples requiring strong bedding planes, each layer was cast with a 60-minute interval. For samples with weak bedding planes, a 120-minute interval was used. Upon completion of the waiting period, the next detachable steel bar was installed, and the above procedures were repeated until all rock layers were cast.

Curing. The cast SHIRLs were left to harden in their molds for 24 hours at room temperature. Subsequently, they were demolded and transferred to a standard curing room maintained at approximately 90% relative humidity and 20 ± 1°C for 28 days. The two types of prepared SHIRL samples are shown in Fig. 3.

To characterize the mechanical parameters of the hard and soft rock layers, as well as the strength of the strong and weak bedding planes, three types of samples were prepared according to the suggested methods of Fairhurst and Hudson (1999): standard cylindrical samples (100 mm height × 50 mm diameter), Brazilian disc samples (50 mm diameter × 20 mm thickness), and cubic composite samples (100 mm length × 100 mm width × 100 mm total height). The results of the mechanical tests on the soft and hard rocks are presented in Figs. 4(a) and 4(b), with the corresponding basic mechanical parameters listed in Table 2. The shear strength of the strong and weak bedding planes is shown in Fig. 4(c). The experimental results confirm that the mechanical properties of the soft and hard rocks conform to the classification criteria for such rocks established by the International Society for Rock Mechanics (ISRM) (Saroglou and Tsiambaos 2007).

2.1.3 Loading system and DIC system

The TPB tests on the SHIRLs were conducted using an MTS-793 rock mechanics testing system, with a load capacity ranging from -200 kN to +200 kN. As illustrated in Fig. 5, the system primarily consists of a data-acquisition unit (Fig. 5(a)) and the testing machine itself (Fig. 5(b)). The tests were performed under displacement-controlled conditions at a constant rate of 0.15 mm/min. Load-displacement curves were recorded by the machine's internal deformation measurement system, which has an accuracy of 0.001 N for load and 0.001 mm for displacement. The sample dimensions for the TPB tests are provided in Fig. 5(d).

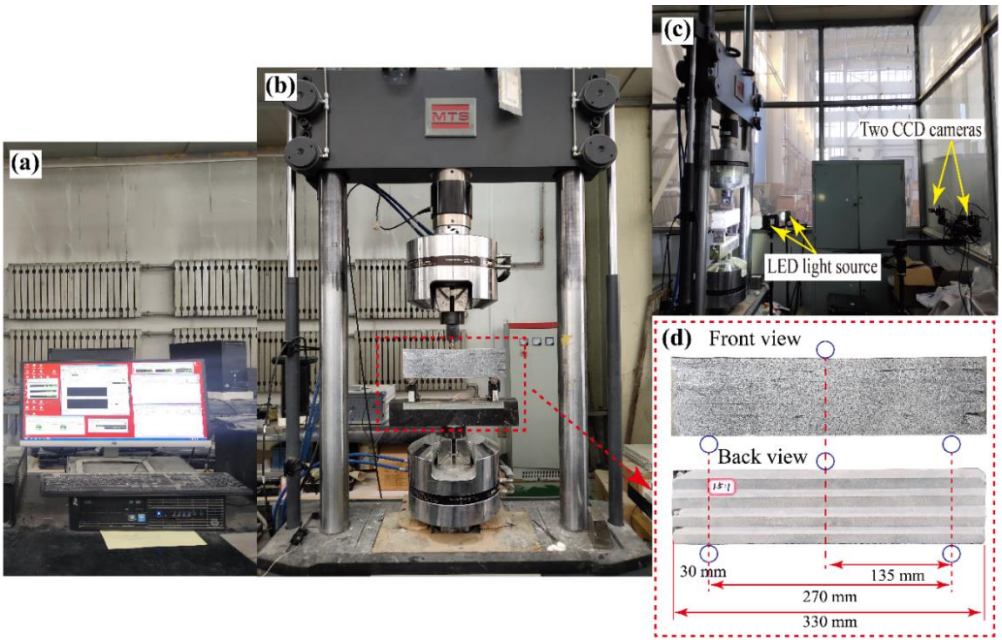

Fig. 5 The main experimental equipment: (a) data acquisition system, (b) loading system, (c) DIC testing system and (d) the loading size of the tested SHIRL

DIC was employed as a non-contact method to measure deformation. This technique is highly sensitive to surface strain changes and is effective for monitoring crack initiation, propagation, and coalescence in rocks and rock-like materials (Munoz *et al*. 2016, Modiriasari *et al*. 2017, Kramarov *et al*. 2020). The DIC system comprised two charge-coupled device (CCD) cameras (Basler/piA2400-17gm) and a VIC-3D image analysis system (Correlated Solutions, Columbia, SC, USA) (Fig. 5(c)). The cameras captured images at a rate of 15 frames per second with a resolution of 2456 × 2058 pixels. The fundamental principles of DIC are well-documented by Schreier *et al*. (2009). To prepare the samples for DIC analysis, a speckle pattern was applied to the surface of the SHIRLs. The surface was first smoothed to ensure it was as flat as possible. A uniform base layer of white paint was then applied and allowed to dry for 30 minutes. Finally, a random and even distribution of black speckles was created by spraying black paint over the white base layer (Fig. 5(d)).

2.2 Numerical simulation

2.2.1 Parallel bond model

As illustrated in Fig. 6(a), the parallel bond model can be conceptualized as a set of springs with constant normal and tangential stiffness, uniformly distributed on the contact plane. This model enables the transmission of both forces and moments between adjacent particles. The contact force is linearly related to the particle overlap and is governed by the bond stiffness and the stiffness ratio. During simulation, if the maximum contact stress exceeds the corresponding bond strength, the parallel bond fails and is removed, causing the model to transition to a linear, unbonded state (Fig. 6(b)). In this unbonded state, particles can rotate freely relative to one another, and shear slip between particles is governed by the Mohr-Coulomb strength criterion. When adjacent particles are in a bonded state, the parallel bonding contact force and moment can be calculated as follows (Dou *et al*. 2019, Potyondy and Cundall 2004).

$$\begin{cases} F_c = F_l + F_d + \bar{F}^{pb} \\ M_c = \bar{M}^{pb} \end{cases} \tag{1}$$

where F_c is contact force between particles, M_c is the moment between particles, F_l is the linear force, F_d is the dashpot force, and $\bar{F}^{pb}$ is the parallel-bond force, $\bar{M}^{pb}$ is the bending moment in the parallel bond model.

During the calculation process, the parallel bonded force and the moment are updated as

$$\begin{cases} \bar{F}^{pb} = \bar{F}_n^{pb} + \bar{F}_s^{pb} \\ \bar{F}_n^{pb} = \bar{F}_n^{pb} + \bar{K}_n^{pb} A \Delta\delta_n \\ \bar{F}_s^{pb} = \bar{F}_s^{pb} - \bar{K}_s^{pb} A \Delta\delta_s \end{cases} \tag{2}$$

where A is the area of adjacent particles contact plane, $\bar{K}_n^{pb}$ and $\bar{K}_s^{pb}$ are the normal and shear stiffness in per unit area, respectively. The δ_n and δ_s are the relative increment of normal and shear displacement.

The maximum normal and shear stresses acting on the parallel bond are updated by

$$\bar{\sigma}_{\max} = \frac{\bar{F}_n^{pb}}{A} + \beta \frac{\bar{M}^{Pb} \bar{R}}{I}, \bar{\tau}_{\max} = \frac{\bar{F}_s^{pb}}{A} \tag{3}$$

$$\begin{cases} \bar{\sigma}_{\max} > \bar{\sigma}_c, \quad \bar{\sigma} = 0 & \text{tensile crack} \\ \bar{\tau}_{\max} > \bar{\tau}_c, \bar{\tau} = \bar{c} + \bar{\sigma} \tan\varphi & \text{shear crack} \end{cases} \tag{4}$$

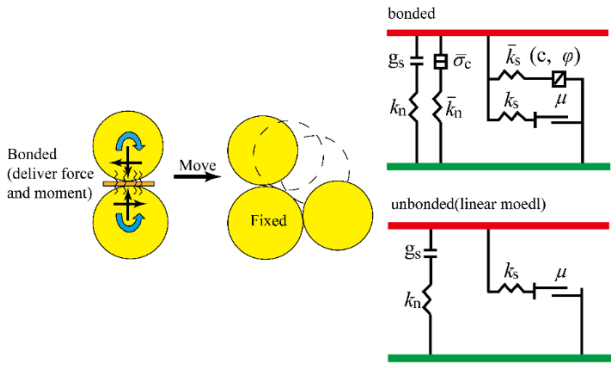

(a) Particle motion (b) Rheological components

Fig. 6 Parallel bond model (Potyondy and Cundall 2004, Dou *et al*. 2019, PFC manual, version 5.0)

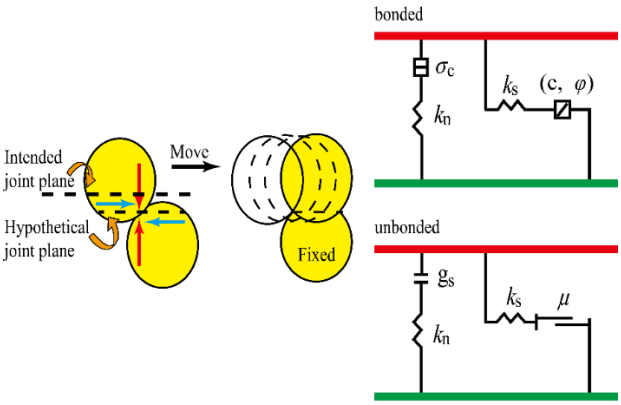

(a) Particle motion (b) Rheological components

Fig. 7 Smooth joint model (Pierce *et al*. 2007, Dou *et al*. 2019, PFC manual, version 5.0)3. Test results

where $\bar{\sigma}_c$ and $\bar{\tau}_c$ are the tensile and shear strength of parallel bond model, $\bar{c}$ is the cohesion strength at per unit area, β is the moment contribution factor.

2.2.2 Discrete fracture network and smooth joint model

The parallel bond model effectively simulates the mechanical behavior of intact rock by representing the bonds between particles. In layered composite rocks containing multiple bedding planes, the mechanical properties of these planes significantly influence the overall mechanical response and failure modes of the rock mass. Within the PFC^{2D} environment, the Discrete Fracture Network (DFN) module provides an efficient tool for generating and managing fractures. This module represents a fracture population embedded in a rock mass as a set of discrete, planar, finite-sized fractures. A core function of the DFN is to define the mechanical properties of fracture planes and to create smooth-joint contacts. The smooth-joint model simulates the behavior of an interface without being influenced by the local orientation of particle contacts along that interface (Fig. 7(a)). In practice, for the bedding planes in the numerical samples, the parallel bonds at the particle interfaces were replaced with smooth-joint contacts. By modifying the bond states and mechanical parameters of the smooth-joint model, the mechanical behavior and failure mechanisms of the bedding planes can be accurately simulated. It is worth noting that in the bonded state, the mechanical behavior of the smooth-joint model is linearly elastic until the contact strength reaches its peak value. Once the contact strength exceeds this maximum, the model transitions from a bonded to an unbonded state (Fig. 7(b)). In this unbonded state, the mechanical behavior is governed by a frictional law, analogous to the post-failure behavior of the parallel bond model.

The formula of smooth joint model as shown in Eq. (5), and its force is updated by the Eq. (6) (Dou *et al*. 2019, Pierce *et al*. 2007)

$$\bar{\sigma}_{\max} = \frac{\bar{F}_n^{sj}}{A}, \bar{\tau}_{\max} = \frac{\bar{F}_s^{sj}}{A} \tag{7}$$

$$\begin{cases} \bar{\sigma}_{\max} > \bar{\sigma}_c^{sj}, \bar{F}_n^{sj} = \bar{F}_s^{sj} = 0 & \text{tensile} \\ \bar{\tau}_{\max} > \bar{\tau}_c^{sj}, \bar{F}_n^{sj} = \bar{F}_s^{sj} + \left(\dfrac{\bar{F}_s^{sj} - \bar{F}_s^{\mu}}{\bar{K}_s^{sj}} \right) \cdot \bar{K}_n^{sj} \cdot \tan\varphi & \text{shear} \end{cases} \tag{8}$$

where $\bar{\sigma}_c^{sj}$ and $\bar{\tau}_c^{sj}$ are the normal and shear strength of smooth-joint bond, φ is the dilation angle on the bedding plane.

3.1 Load-displacement curves

The load-displacement curves for the SHIRLs are presented in Figs. 8 and 9. These curves can be categorized into four distinct stages: initial deformation, elastic deformation, instantaneous fracture, and post-peak behavior. As shown in Fig. 8, for SHIRLs with strong bedding planes, an increasing thickness ratio reduces the proportion of the initial deformation stage while extending the elastic stage. This trend indicates that a thicker soft rock layer leads to a more pronounced initial deformation and a delayed transition into the elastic stage. Conversely, a thicker hard rock layer minimizes the initial deformation and facilitates a quicker transition to elastic deformation. Upon failure, the load drops abruptly. It does not fall directly to zero but stabilizes at a low residual value until the sample fractures completely.

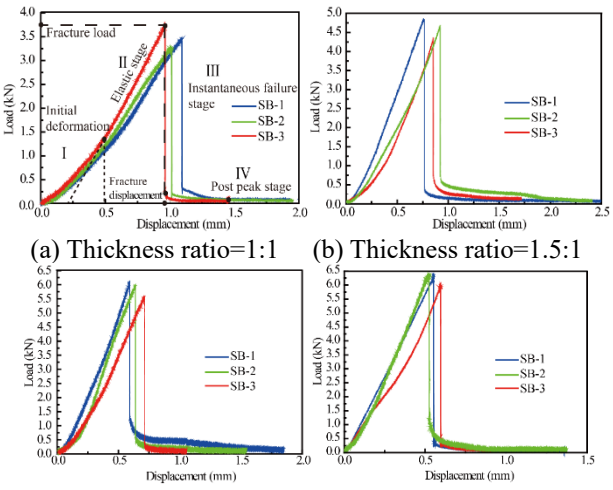

(a) Thickness ratio=1:1 (b) Thickness ratio=1.5:1

(c) Thickness ratio=2:1 (d) Thickness ratio=2.5

Fig. 8 The load-displacement curves of SHIRLs with strong bedding plane strength

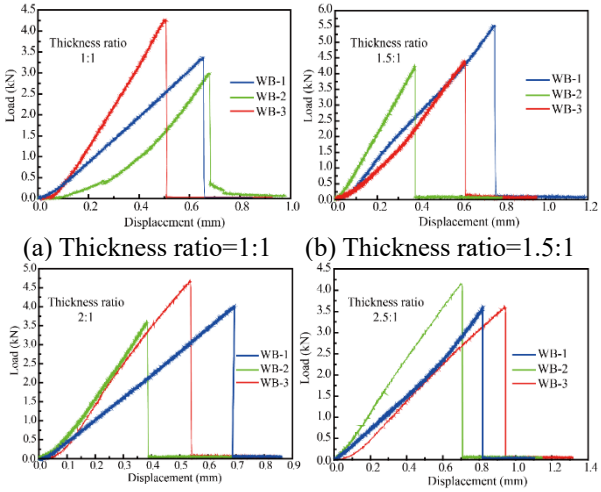

(a) Thickness ratio=1:1 (b) Thickness ratio=1.5:1

(c) Thickness ratio=2:1 (d) Thickness ratio=2.5:1

Fig. 9 The load-displacement curves of SHIRLs with weak bedding plane strength

Furthermore, strong bedding plane strength reduces the dispersion in fracture load and displacement. For these samples, the fracture load and displacement are primarily governed by the thickness ratio. Fig. 9 displays the load-displacement curves for SHIRLs with weak bedding plane strength. Under identical thickness ratio conditions, these curves exhibit significant variability. Both the fracture load and displacement show obvious dispersion. When these samples fail, the load drops sharply to a value near zero.

3.2 Fracture load and fracture displacement

The fracture load and displacement for SHIRLs with strong bedding planes are presented in Fig. 10. As shown in Figs. 10(a) and 10(b), the fracture load increases linearly with the thickness ratio, whereas the fracture displacement decreases linearly. This linear relationship occurs because the strong bedding planes cause the SHIRL to behave as a cohesive, composite unit. Within this unit, the hard rock layers possess high strength and density with low deformability, while the soft rock layers have lower strength and density and are more prone to deformation. Consequently, the thickness ratio directly governs the mechanical response, dictating that a higher proportion of hard rock leads to a greater fracture load and a smaller fracture displacement. Conversely, a higher proportion of soft rock results in a larger fracture displacement and a smaller fracture load. These trends demonstrate that strong bedding planes effectively control the fracture behavior, minimizing data dispersion.

In contrast, Figs. 11(c) and 11(d) present the fracture load and displacement for SHIRLs with weak bedding planes. Here, the fracture load initially increases and then decreases with the thickness ratio, while the fracture displacement shows an inverse trend. Furthermore, under identical thickness ratios, the fracture load and displacement exhibit significant data scatter. This indicates that the weak bedding plane strength is the primary cause of the pronounced dispersion in the results. The inability of the weak planes to effectively bond the hard and soft layers leads to unpredictable, random fracture paths during bending tests.

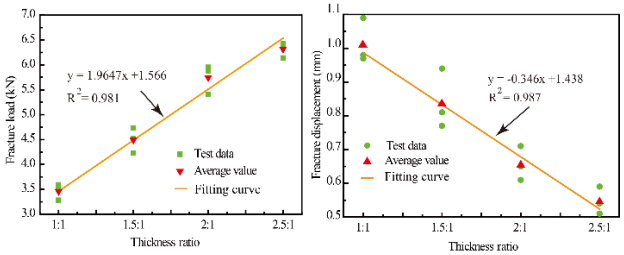

(a) Fracture load (b) Fracture displacement

Fig. 10 The fracture load and displacement of SHIRLs with strong bedding plane strength

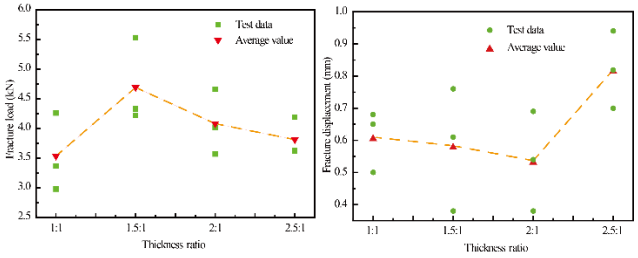

(a) Fracture load (b) Fracture displacement

Fig. 11 The fracture load and displacement of SHIRLs with weak bedding plane strength

3.3 Fracture process

The fracture process of SHIRLs with strong bedding planes is illustrated in Fig. 12. The thickness ratio has no significant influence on the fracture process, which consistently features a single main crack. This crack initiates at the bottom of the sample and propagates upward. At the point of fracture, the instantaneous length of the main crack is approximately half the total height of the SHIRL, a measurement unaffected by the thickness ratio. Following the initial fracture, the load decreases gradually as the main crack continues to develop slowly. This indicates that the SHIRLs retain a residual load-carrying capacity until complete failure occurs.

In contrast, the fracture process for SHIRLs with weak bedding planes, shown in Fig. 13, is significantly influenced by the thickness ratio. At a thickness ratio of 1:1, the process is similar to that of SHIRLs with strong bedding planes, with a main crack extending to about half the sample's height. However, at ratios of 1.5:1 and 2:1, the instantaneous fracture lengths of the main crack are approximately five-sixths and eight-ninths of the total sample height, respectively. Furthermore, all SHIRLs with weak bedding planes develop bedding cracks during bending. The location and extent of these bedding cracks vary considerably with the thickness ratio.

3.4 Ultimate failure pattern

The ultimate failure patterns of the two types of SHIRLs are compared in Fig. 14. The main crack, which initiates at the bottom and propagates upward, tapers in width from bottom to top. These cracks are not parallel to the direction of the principal stress but instead form an acute angle with it. SHIRLs with strong bedding planes exhibit almost no bedding cracks.

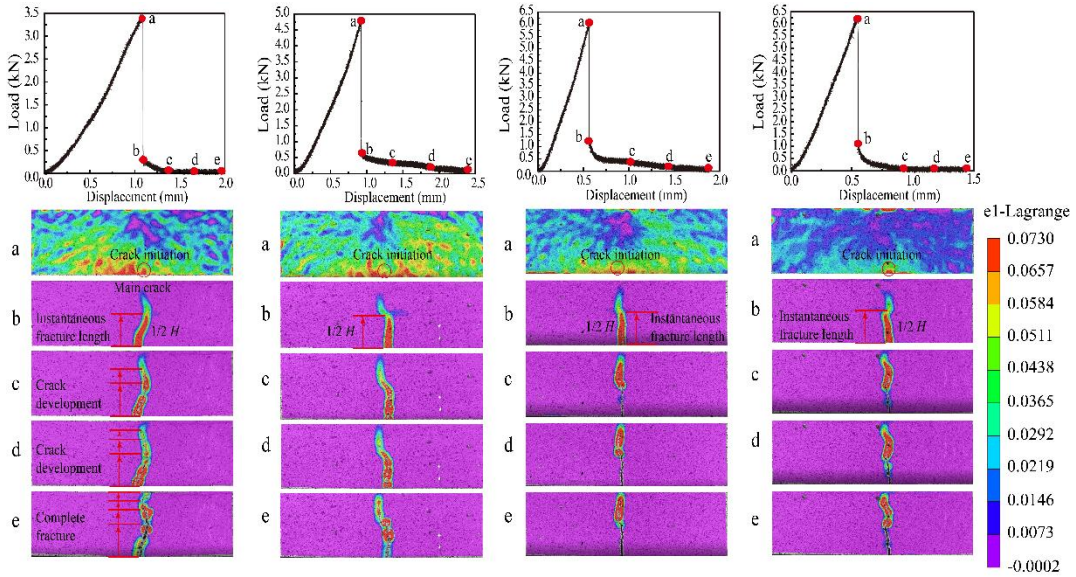

(a) Thickness ratio=1:1 (b) Thickness ratio=1.5:1 (c) Thickness ratio=2:1 (d) Thickness ratio=2.5:1

Fig. 12 The fracture process of SHIRLs with strong bedding plane strength

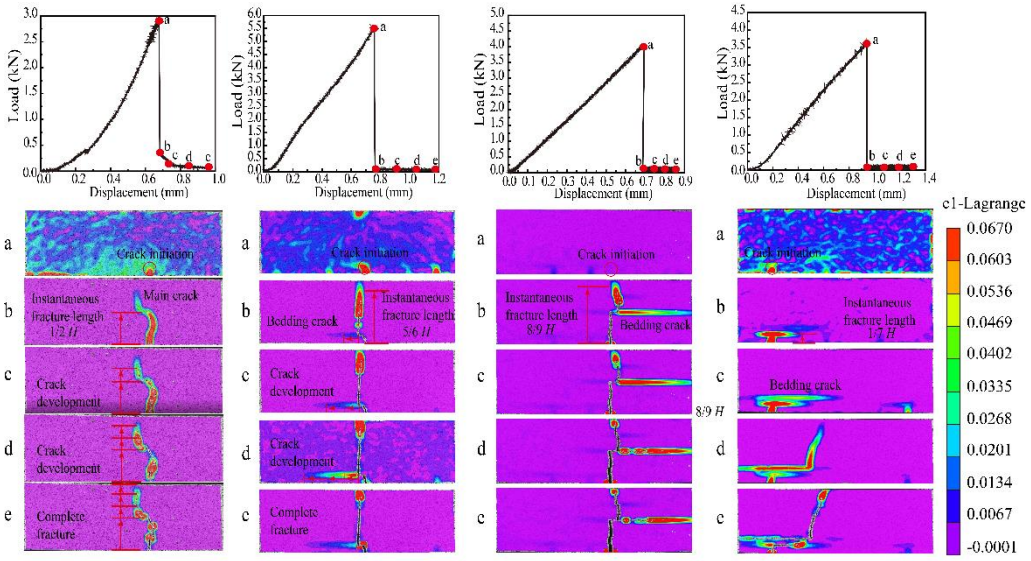

(a) Thickness ratio=1:1 (b) Thickness ratio=1.5:1 (c) Thickness ratio=2:1 (d) Thickness ratio=2.5:1

Fig. 13 The fracture process of SHIRLs with weak bedding plane strength

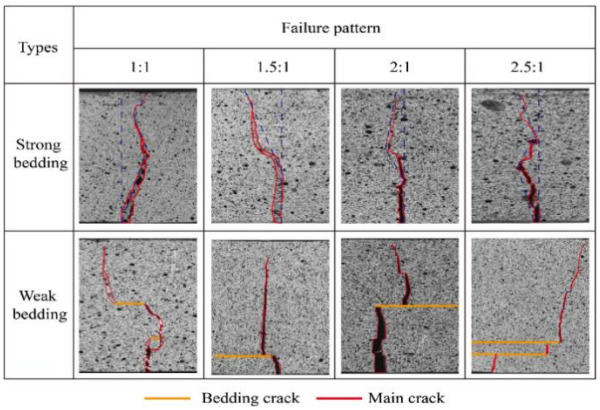

Fig. 14 The ultimate failure patterns of two types of SHIRLs

In contrast, SHIRLs with weak bedding planes develop prominent bedding cracks. The presence of these bedding cracks causes significant deflection of the main crack, facilitating a more extensive crack propagation path.

4. Numerical results

4.1 Numerical model and calibration of micro-parameters

The numerical model, shown in Fig. 15, replicates the geometry of the tested SHIRLs. The particle sizes range from 0.32 mm to 0.48 mm in diameter, and the initial porosity is set

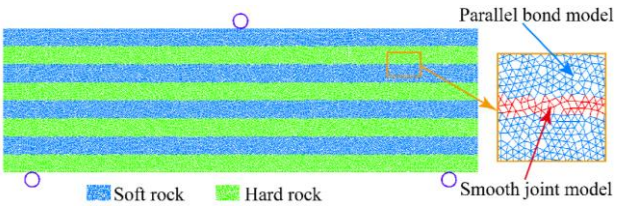

Fig. 15 The numerical model of SHIRL (thickness ratio=1:1)

Table 3 Micro-parameters of rock layers used in the PFC^{2D} model

Micro-parameter Value	Types	
	Hard rock	Soft rock
Particle density (kg/m^3)	2500	2300
Ratio of particle radius	1.5	1.5
Ratio of normal to shear stiffness of the parallel bond	1.2	1
Yong's modulus of the particle (GPa)	1.5	0.8
Particle friction coefficient	0.5	0.5
Tensile strength of the parallel bond (MPa)	0.12	0.1
Shear strength of the parallel bond (MPa)	1.5	1.2

Table 4 Micro-parameters of bedding plane used in the PFC^{2D} model

Micro-parameter Value	Value
Normal stiffness of smooth joint (GPa/m)	35
Shear stiffness of smooth joint (GPa/m)	35
Tensile strength of smooth joint (MPa)	1.5
Shear strength of smooth joint (MPa)	2.0
Friction coefficient	0.5

to 3% to minimize boundary effects. Each model contains 31,163 particles, resulting in approximately 84,802 contacts. For PFC^{2D} modeling, the micro-parameters for the bedding planes and rock matrix cannot be obtained directly from experiments. Therefore, a "trial and error" approach, a practical and validated method, was employed to calibrate these parameters (Guo *et al*. 2020). The calibration procedure was as follows: First, the macro-mechanical properties were determined through a series of laboratory tests, and a numerical model with identical dimensions was constructed. The micro-parameters were then iteratively adjusted until key simulation results-namely, the load-displacement curve slope (generalized stiffness), peak load, and fracture pattern-closely matched the experimental data. The iterative process concluded when the discrepancies between the numerical and experimental results fell within an acceptable margin. The final calibrated micro-parameters for the hard rock, soft rock, and bedding planes are listed in Tables 3 and 4, respectively.

4.2 Comparative analysis between experimental and numerical results

A comparison of the numerical and experimental load-displacement curves for SHIRLs with strong bedding planes is presented in Fig. 16. The experimental curves exhibit a non-linear initial deformation stage, attributable to the closure of inherent microscopic defects such as microcracks and pores. While replicating this initial non-linearity is challenging in the numerical model, the simulation shows strong agreement with the experimental data during the elastic deformation stage, at peak load, and in the post-peak brittle failure process. The error between the experimental average fracture load and the simulated value is less than 15%, confirming that the numerical model accurately captures the variation in peak load across different layer thickness ratios. The simulated ultimate failure pattern, also shown in Fig. 16, corresponds well with the experimental observations from Fig. 14, further validating the model's reliability. These results demonstrate that the PFC^{2D} models effectively capture the fracture behavior of SHIRLs. It is noteworthy that the numerical simulation in Fig. 16 shows no shear-slip at the bedding planes, with the load-displacement curve remaining largely linear-elastic. A probable explanation is that the assigned shear stiffness, normal stiffness, and strength of the bedding planes were sufficiently high, preventing the shear stress from reaching the critical threshold required for slip initiation.

4.3 Effect of bedding plane strength on the fracture load and failure pattern

To further explore the effect of bedding plane strength on the bending fracture behavior of the SHIRLs under the TPB test, change the tensile and shear strength of the bedding plane simultaneously with strength ratios of 0.9, 0.85, 0.8, 0.75, 0.7, 0.65, 0.6, 0.55, 0.5, 0.45 and 0.4 to the calibrated bedding plane strength listed in Table 4, and all the other parameters shown in Table 4 remain the same. The eleven sets of parameters on bedding plane strength were obtained and adopted in the simulation.

4.3.1 Fracture load

The influence of bedding plane strength on fracture load is presented in Fig. 17. The fracture load for all SHIRLs decreases with reducing bedding plane strength. The relationship between bedding plane strength and fracture load under TPB tests can be categorized into three distinct segments. The fracture load differs markedly between these segments but exhibits minimal variation within each segment.

It is noteworthy that SHIRLs with different layer thickness ratios exhibit different sensitivities to changes in bedding plane strength. For a thickness ratio (hard rock to soft rock) of 1:1, the corresponding bedding plane strength ratios for the three segments are 0.4-0.6, 0.65-0.75, and 0.8-0.9. In contrast, for a thickness ratio of 2.5:1, the corresponding strength ratios are 0.4-0.65, 0.7-0.85, and 0.9. Furthermore, for an identical bedding plane strength ratio, a larger rock layer thickness ratio results in a higher fracture load.

4.3.2 Failure pattern

The numerical failure patterns of SHIRLs with varying bedding plane strengths are illustrated in Fig. 18. Based on the variation in bedding plane strength, the failure patterns can be categorized into three types. When the bedding plane strength ratio ranges from 0.8 to 0.9, the bedding planes exert

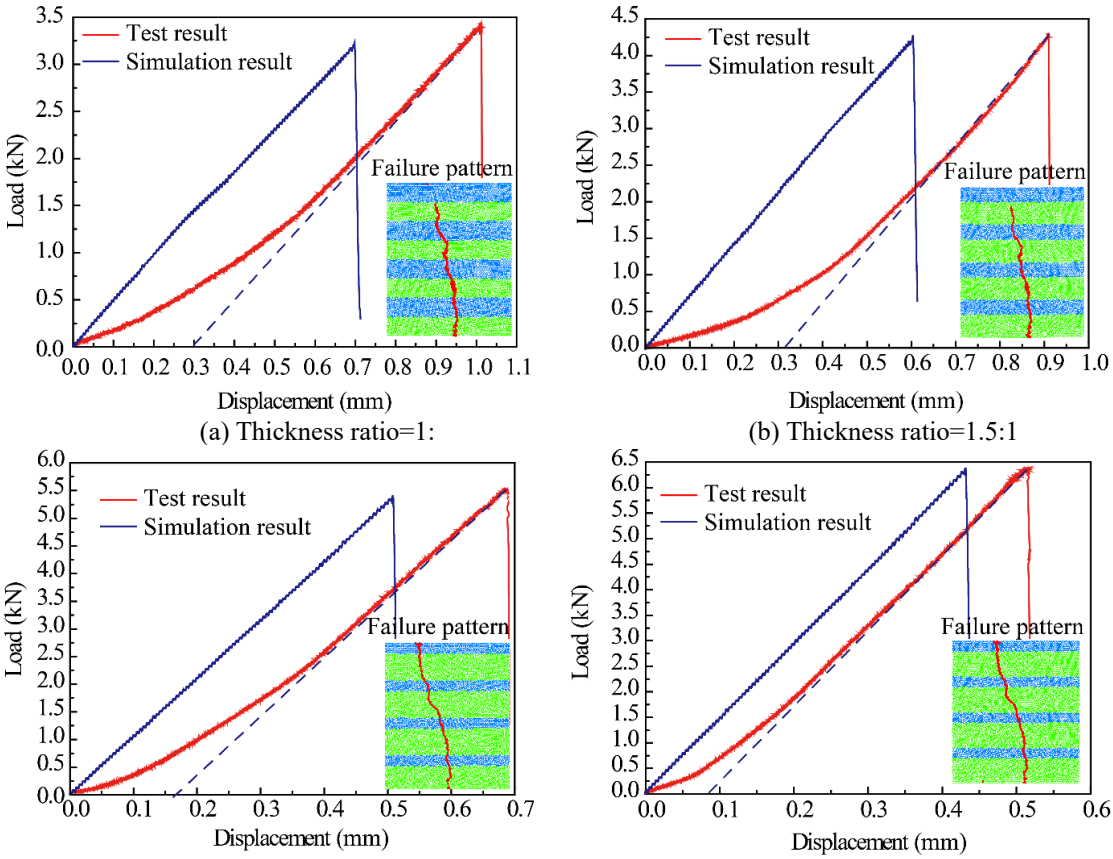

Fig. 16 Comparisons between numerical and experimental load-displacement curves of SHIRLs with strong bedding plane strength under three-point-bending test

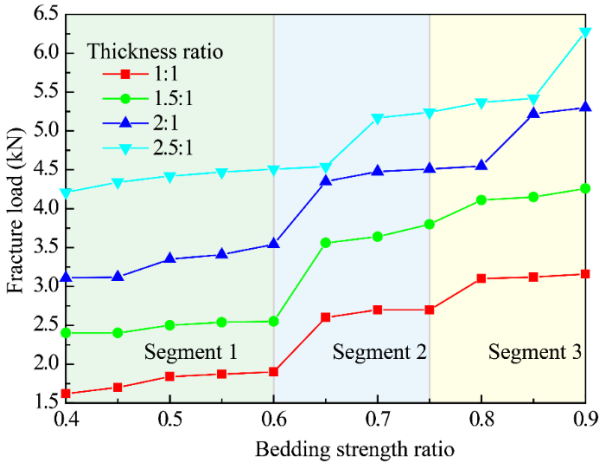

Fig. 17 Effect of bedding plane strength on the fracture load of SHIRLs

negligible influence on the failure pattern, with few to no bedding cracks (shear cracks) observed. As the bedding plane strength ratio decreases to a range of 0.6-0.85, its influence on the failure pattern becomes more pronounced, and the number of bedding cracks increases. When the strength ratio falls within the range of 0.4-0.65, numerous bedding cracks develop. Furthermore, SHIRLs with a higher thickness ratio of hard to soft rock are more sensitive to changes in bedding plane strength.

Consequently, a larger rock layer thickness ratio makes the specimen more susceptible to bedding crack formation as the bedding plane strength decreases. This occurs because a higher thickness ratio compromises the coordinated deformation ability between the hard and soft rock layers. The effect of bedding plane strength on the proportion of tensile and shear cracks is shown in Fig. 19. For all SHIRLs, a decrease in bedding plane strength leads to an increase in the number of shear cracks (bedding cracks), while the number of tensile cracks (constituting the main crack) remains relatively constant. Therefore, as the bedding plane strength decreases, the proportion of shear cracks increases, and the proportion of tensile cracks decreases correspondingly.

5. Conclusions

This study investigated the influence of bedding plane strength on the bending fracture behavior of SHIRLs by integrating TPB tests, DIC, and PFC^{2D} simulations. The principal conclusions are as follows:

- Bedding plane strength is a decisive factor controlling the bending fracture behavior of SHIRLs, governing the load-displacement curves, fracture load, fracture displacement, fracture process, and ultimate failure pattern.
- For SHIRLs with strong bedding planes, the fracture load

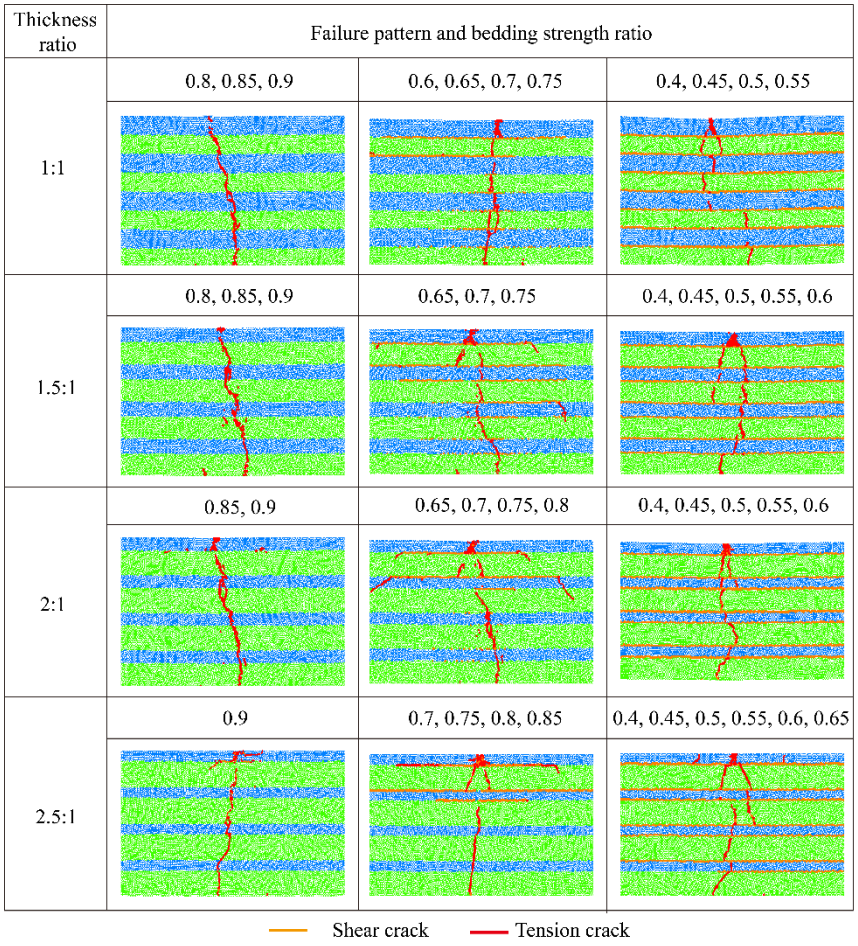

Fig. 18 Numerical failure patterns of SHIRLs with different bedding plane strength

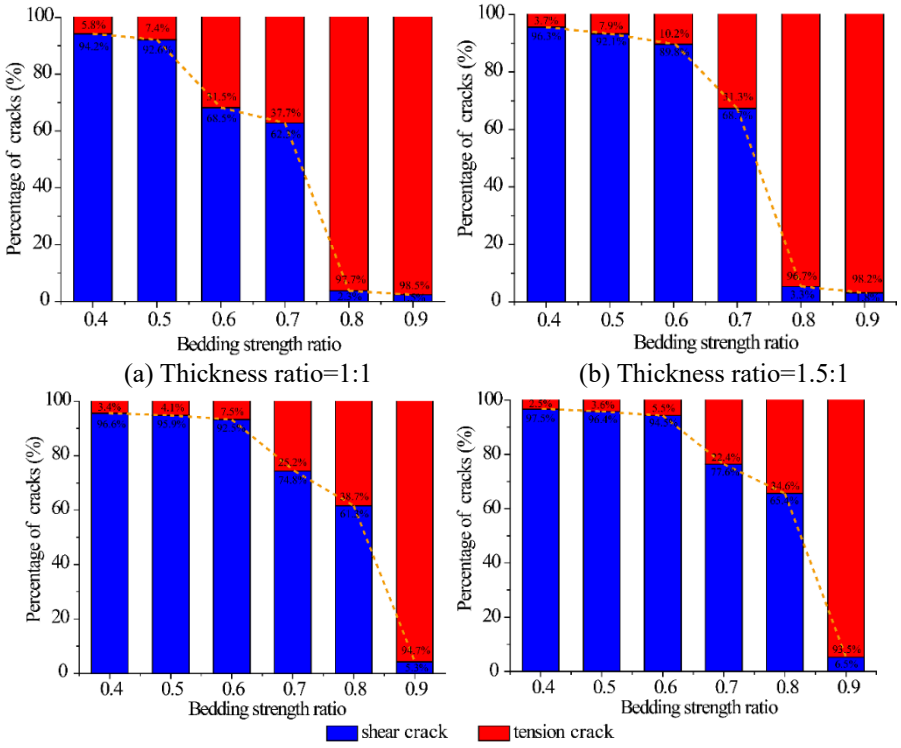

(a) Thickness ratio=1:1 (b) Thickness ratio=1.5:1

(c) Thickness ratio=2:1 (d) Thickness ratio=2.5:1

Fig. 19 Effect of bedding plane strength on the percentage of cracks of SHIRLs

increases linearly with the rock layer thickness ratio, while the fracture displacement decreases linearly. The instantaneous fracture length of the main crack is approximately half the total sample height, and interlayer cracks are rarely observed. In contrast, for SHIRLs with weak bedding planes, the load-displacement curves, fracture load, fracture displacement, fracture process, and ultimate failure pattern all exhibit significant dispersion. These failures are consistently accompanied by the development of bedding cracks.

- The parallel bond and smooth-joint models in PFC^{2D} effectively simulate the bending fracture behavior of soft-hard interbedded rock layers (SHIRLs) under three-point-bending (TPB) tests. Based on the bedding plane strength, the fracture response can be categorized into three distinct types. For the first type (strength ratios are 0.8-0.9), the fracture load and pattern are very similar to those of SHIRLs with strong bedding planes. Cracks are predominantly tensile (forming the main crack), with almost no shear (bedding) cracks. For the second type (strength ratios are 0.6-0.85), the fracture load decreases, and shear (bedding) cracks increase noticeably. For the third type (strength ratios are 0.4-0.65), the fracture load decreases further, accompanied by a substantial increase in shear (bedding) cracks.

It is noteworthy that changes in the intrinsic mechanical properties of the hard and soft rocks can also influence the bending fracture of SHIRLs. Therefore, future work will focus on investigating the effect of these rock properties on the fracture behavior.

Acknowledgments

The present work is supported by the Key Program of National Natural Science Foundation of China (No. U23A2047), the National Natural Science Foundation of China (No. 42277187), the Sichuan Science and Technology Program (No. 2025ZNSFSC1210), and the Key R&D Project of Deyang Science and Technology Plan (No. 2024SZZ181), the Sichuan Polytechnic University Key Research Project (No. XJ2025KJ-10).

References

Alitalesh, M., Yazdani, M., Fakhimi, A. and Naeimabadi, M. (2020), "Effect of loading direction on interaction of two pre-existing open and closed flaws in a rock-like brittle material", *Undergr. Sp.*, **5**(3), 242-257. https://doi.org/10.1016/j.undsp.2019.04.003.

Chen, J., Liu, W. and Chen, L. (2020), "Failure mechanisms and modes of tunnels in monoclinic and soft-hard interbedded rocks: a case study", *KSCE J. Civ. Eng.*, **24**(4), 1357-1373. https://doi.org/10.1007/s12205-020-1324-3.

Dong, M.L. and Zhang, F.M. (2020a), "Study on deformation and failure law of soft-hard rock interbedding toppling slope base on similar test", *Bull. Eng. Geol. Environ.*, **79**(9), 4625-4637. https://doi.org/10.1007/s10064-020-01845-4.

Dong, M.L., Zhang, F.M. and Hu, M.J. (2020b), "Study on the influence of anchorage angle on the anchorage effect of soft-hard interbedded toppling deformed rock mass", *KSCE J. Civ. Eng.*, **24**, 2382-2392. https://doi.org/10.1007/s12205-020-2386-y.

Doolin, D.M. and Mauldon, M. (2001), "Fracture permeability normal to bedding in layered rock masses", *Int. J. Rock Mech. Min. Sci.*, **38**(2), 199-210. https://doi.org/10.1016/S1365-1609(00)00056-3.

Dou, F.K., Wang, J.G. and Zhang, X.X. (2019), "Effect of joint parameters on fracturing behavior of shale in notched three-point-bending test based on discrete element model", *Eng. Fract. Mech.*, **205**, 40-56. https://doi.org/10.1016/j.engfracmech.2018.11.017.

Fairhurst, C.E. and Hudson, J.A. (1999), Draft isrm suggested method for the complete stress train curve for the intact rock in uniaxial compression, *Int. J. Rock Mech. Min. Sci.*, **36**(3), 279-289. https://doi.org/10.1016/S0148-9062(99)00006-6.

Gu, D.M. and Huang, D. (2016), "A complex rock topple-rock slide failure of an anaclinal rock slope in the Wu Gorge, Yangtze River, China", *Eng. Geol.*, **208**, 165-180. https://doi.org/10.1016/j.enggeo.2016.04.037.

Guo, W.B., Hu, B., Cheng, J.L. and Wang, B.F. (2020), "Modeling time-dependent behavior of hard sandstone using the DEM method", *Geomech. Eng.*, **20**(6), 517-525. https://doi.org/10.12989/gae.2020.20.6.517.

Guo, W.Y., Tan, Y.L., Yu, F.H., Zhao, T.B., Hu, S.C., Huang, D.M. and Qin, Z. (2018), "Mechanical behavior of rock-coal-rock specimens with different coal thicknesses", *Geomech. Eng.*, **15**(4), 1017-1027. https://doi.org/10.12989/gae.2018.15.4.1017.

Haeri, H., Khaloo, A. and Marji, M.F. (2015), "Experimental and numerical simulation of the microcrack coalescence mechanism in rock-like materials", *Strength Mater.*, **47**, 740-754. https://doi.org/10.1007/s11223-015-9711-6.

Hu, B., Yang, S.Q., Xu, P. and Cheng, J.L. (2019), "Cyclic loading-unloading creep behavior of composite layered specimens", *Acta. Geophys.*, **67**(2), 449-464. https://doi.org/10.1007/s11600-019-00261-x.

Huang, D., Li, B. and Ma, W.Z. (2020), "Effects of bedding planes on fracture behavior of sandstone under semicircular bending test", *Theor. Appl. Fract. Mech.*, **108**, 102625. https://doi.org/10.1016/j.tafmec.2020.102625.

Khalili, M., Fahimifar, A. and Shobeiri, H. (2023), "The effect of bedding planes on the bending strength of rock-like material and evaluation of the crack propagation mechanism", *Theor. Appl. Fract. Mech.,* **127**, 104061. https://doi.org/10.1016/j.tafmec.2023.104061.

Kramarov, V., Parrikar, P.N. and Mokhtari, M. (2020), "Evaluation of fracture toughness of sandstone and shale using digital image correlation", *Rock Mech. Rock Eng.*, **53**, 4231-4250. https://doi.org/10.1007/s00603-020-02171-7.

Kumar, S., Tiwari, G., Parameswaran, V. and Das, A. (2023), "Dynamic mechanical behaviour of rock-like materials with a flaw under different orientation and infill conditions", *Bull. Eng. Geol. Environ.*, **82**, 345. https://doi.org/10.1007/s10064-023-03365-3.

Lee, G.J., Ryu, H.H., Cho, G.C. and Kwon, T.H. (2023), "Full-scale TBM excavation tests for rock-like materials with different uniaxial compressive strength", *Geomech. Eng.*, **35**(5), 487-497. https://doi.org/10.12989/gae.2023.35.5.487.

Liu, J., Yao, K. and Xue, Y. (2019), "Study on fracture behavior of bedded shale in three-point-bending test based on hybrid phase-field modelling", *Theor. Appl. Fract. Mech.*, **104**, 102382. https://doi.org/10.1016/j.tafmec.2019.102382.

Luo, G.Y., Yang, W.D., Bo, C.J. and Zhang, L.Z. (2021), "Viscoelastic analysis of the creep characteristics of interlayered rock specimens under uniaxial compression", *Mech. Time-Depend Mater*, **25**, 37-60. https://doi.org/10.1007/s11043-019-09441-0.

Meier, S., Bauer, J.F. and Philipp, S.L. (2017), "Fault zones in layered carbonate successions: from field data to stress field models", *Geomech. Geophys. Geo-energ. Geo-resour.*, **3**, 61-93. https://doi.org/10.1007/s40948-016-0047-x.

Modiriasari, A., Bobet, A. and Pyrak-Nolte, L.J. (2017), "Active seismic monitoring of crack initiation, propagation, and coalescence in rock", *Rock Mech. Rock Eng.*, **50**, 2311-2325. https://doi.org/10.1007/s00603-017-1235-x.

Mohammadi, M. and Hossaini, M.F. (2017), "Modification of rock mass rating system: Interbedding of strong and weak rock layers", *J. Rock Mech. Geotech. Eng.*, **9**(6), 1165-1170. https://doi.org/10.1016/j.jrmge.2017.06.002.

Munoz, H., Taheri, A. and Chanda, E.K. (2016), "Pre-peak and post-peak rock strain characteristics during uniaxial compression by 3D digital image correlation", *Rock Mech. Rock Eng.*, **49**, 2541-2554. https://doi.org/10.1007/s00603-016-0935-y.

Pierce, M., Ivars, D.M., Potyondy, D.O. and Cundall, P.A. (2007), "A Synthetic Rock Mass Model for Jointed Rock", in Rock Mechanics: Meeting Society's Challenges and Demands (1st Canada-US Rock Mechanics Symposium, Vancouver, Canada, May 2007), Vol. 1: Fundamentals, New Technologies & New Ideas, 341-349. (Eds., E. Eberhardt, D. Stead and T. Morrison), London: Taylor & Francis Group.

Potyondy, D.O. and Cundall, P.A. (2004), "A bonded-particle model for rock", *Int. J. Rock Mech. Min. Sci.*, **41**(8), 1329-1364. https://doi.org/10.1016/j.ijrmms.2004.09.011.

Saroglou, H. and Tsiambaos, G. (2007), "Classification of anisotropic rocks", ISRM-11CONGRESS-2007-2043, *Proceedings of the 11th ISRM Congress*.

Schreier, H., Orteu, J.J. and Sutton, M.A. (2009), "Image correlation for shape, motion and deformation measurements: basic concepts, theory and applications", Springer Publishing Company, New York, NY, USA.

Sharafisafa, M., Aliabadian, Z., Tahmasebinia, F. and Shen, L.M. (2021), "A comparative study on the crack development in rock-like specimens containing unfilled and filled flaws", *Eng. Frac. Mech.*, **241**, 107405. https://doi.org/10.1016/j.engfracmech.2020.107405.

Singh, P.K., Pradhan, S.P. and Vishal, V. (2024), "Analysis of tensile failure mechanism in intact, foliated, and cracked rocks using distinct element method: Influence of anisotropy", *Eng. Fail Anal.*, **166**, 108859. https://doi.org/10.1016/j.engfailanal.2024.108859.

Son, M. and Adedokun, S. (2017), "Earth pressure on a retaining structure in layered and jointed rock masses", *KSCE J. Civ. Eng.*, **21**, 1147-1153. https://doi.org/10.1007/s12205-016-0402-z.

Terron-Almenara, J., Skretting, E., Holter, K.G. and Høien A.H. (2024), "Design of rock support in hard and layered rock masses using a hybrid method: A study based on the construction of the new Skarvberg Tunnel, Norway", *Rock Mech. Rock Eng.*, **57**, 10491-10532. https://doi.org/10.1007/s00603-024-04082-3.

Wen, S., Zhang, C., Chang, Y. and Hu, P. (2020), "Dynamic compression characteristics of layered rock mass of significant strength changes in adjacent layers", *J. Rock Mech. Geotech. Eng.*, **12**(2), 353-365. https://doi.org/10.1016/j.jrmge.2019.09.003.

Zolfaghari, A., Khamehchiyan, M., Nikudel, M.R. and Sohrabi-Bidar. A. (2024), "Effects of joints on anisotropy of P- wave velocity, particle vibration and rock mass quality in limestone", *Bull. Eng. Geol. Environ.*, **83**, 375. https://doi.org/10.1007/s10064-024-03872-x.